ARL-CR-0852 ● July 2020

Human Response to High-Rate Loading

prepared by Lance Frazer and Daniel P Nicolella
Southwest Research Institute
6220 Culebra Road
San Antonio, TX 78238

under contract W911QX-17-D-0014-0001 / PR 0011062050

NOTICES

Disclaimers

ARL-CR-0852 ● JULY 2020

Human Response to High-Rate Loading

prepared by Lance Frazer and Daniel P Nicolella
Southwest Research Institute
6220 Culebra Road
San Antonio, TX 78238

under contract W911QX-17-D-0014-0001 / PR 0011062050

REPORT DOCUMENTATION PAGE			*Form Approved OMB No. 0704-0188*

Public reporting burden for this collection of information is estimated to average 1 hour per response, including the time for reviewing instructions, searching existing data sources, gathering and maintaining the data needed, and completing and reviewing the collection information. Send comments regarding this burden estimate or any other aspect of this collection of information, including suggestions for reducing the burden, to Department of Defense, Washington Headquarters Services, Directorate for Information Operations and Reports (0704-0188), 1215 Jefferson Davis Highway, Suite 1204, Arlington, VA 22202-4302. Respondents should be aware that notwithstanding any other provision of law, no person shall be subject to any penalty for failing to comply with a collection of information if it does not display a currently valid OMB control number.
PLEASE DO NOT RETURN YOUR FORM TO THE ABOVE ADDRESS.

1. REPORT DATE *(DD-MM-YYYY)*	2. REPORT TYPE	3. DATES COVERED (From - To)
July 2020	Contractor Report	22 September 2017–29 October 2019

4. TITLE AND SUBTITLE
Human Response to High-Rate Loading

5a. CONTRACT NUMBER
W911QX-17-D-0014-0001 / PR 0011062050

5b. GRANT NUMBER

5c. PROGRAM ELEMENT NUMBER

6. AUTHOR(S)
Lance Frazer and Daniel P Nicolella

5d. PROJECT NUMBER

5e. TASK NUMBER

5f. WORK UNIT NUMBER

7. PERFORMING ORGANIZATION NAME(S) AND ADDRESS(ES)
Southwest Research Institute
6220 Culebra Road
San Antonio, TX 78238

8. PERFORMING ORGANIZATION REPORT NUMBER

9. SPONSORING/MONITORING AGENCY NAME(S) AND ADDRESS(ES)
CCDC Army Research Laboratory
ATTN: FCDD-RLW-B
Aberdeen Proving Ground, MD 21005

10. SPONSOR/MONITOR'S ACRONYM(S)
CCDC ARL

11. SPONSOR/MONITOR'S REPORT NUMBER(S)
ARL-CR-0852

12. DISTRIBUTION/AVAILABILITY STATEMENT
Approved for public release; distribution is unlimited.

13. SUPPLEMENTARY NOTES
ORCID ID: Andrew Tonge, 0000-0002-7985-3027

14. ABSTRACT
Anti-vehicular landmines and improvised explosive devices can produce catastrophic lower-extremity injuries. As such, lower-extremity injury prevention is of high concern but requires a better understanding of high-rate impacts and fracture risk. In this study a probabilistic finite-element model of the tibia and talus was developed to produce a fracture risk assessment. We developed a high-fidelity statistical shape and density model of the tibia to investigate the effect of anatomical variability on the risk of injury. A 7.5-kN distal-tibia impact simulation was developed following the methodology of a previously described framework. This 7.5-kN load corresponds to nearly a 10% tibial fracture risk, which was experimentally derived using cadaveric specimens. The probabilistic analysis resulted in a computed risk of fracture of 10% given the 7.5-kN impact force on the distal tibia. Uncertainty and variability in the bone failure strain, material properties, and tibia anatomy substantially influenced fracture risk. The described probabilistic model reproduced experimentally derived fracture risk and can be used as a comprehensive surrogate to cadaveric testing for high-rate distal-tibia impacts. This model can be used for the design of protective equipment, identification of high-risk individuals, and development of novel injury-mitigation strategies.

15. SUBJECT TERMS
probabilistic analysis, injury risk, finite-element analysis, statistical shape modeling, bone fracture, underbody blast

16. SECURITY CLASSIFICATION OF:			17. LIMITATION OF ABSTRACT	18. NUMBER OF PAGES	19a. NAME OF RESPONSIBLE PERSON
					Andrew Tonge
a. REPORT	b. ABSTRACT	c. THIS PAGE			19b. TELEPHONE NUMBER (Include area code)
Unclassified	Unclassified	Unclassified	UU	32	(410) 278-1069

Standard Form 298 (Rev. 8/98)
Prescribed by ANSI Std. Z39.18

Contents

List of Figures

List of Tables

Summary

Anti-vehicular landmines and improvised explosive devices can produce catastrophic lower-extremity injuries. As such, lower-extremity injury prevention is of high concern but requires a better understanding of high-rate impacts and fracture risk. In this study a probabilistic finite-element (FE) model of the tibia and talus was developed to produce a fracture risk assessment and was compared with experimental cadaveric testing. We developed a high-fidelity statistical shape and density model of the tibia to provide a means of generating physiologically plausible anatomies to investigate the effect of anatomical variability on the risk of injury. Probabilistic descriptions of bone material properties for the tibia were taken from literature and internal sources to account for natural variation and uncertainty. A 7.5-kN distal-tibia impact simulation was developed following the methodology of a previously described framework. This 7.5-kN load corresponds to nearly a 10% tibial fracture risk, which was experimentally derived using cadaveric specimens. Using the probabilistic descriptions of anatomy and material properties, a Latin Hypercube probabilistic FE analysis was performed using the 2nd-percentile strain as a failure criterion. The probabilistic analysis resulted in a computed risk of fracture of 10% given the 7.5-kN impact force on the distal tibia. Uncertainty and variability in the bone failure strain, material properties, and tibia anatomy substantially influenced fracture risk. The described probabilistic model reproduced experimentally derived fracture risk and can be used as a comprehensive surrogate to cadaveric testing for high-rate distal-tibia impacts. This model can be used for the design of protective equipment, identification of high-risk individuals, and development of novel injury-mitigation strategies.

1. Introduction

Anti-vehicular landmines and improvised explosive devices (IEDs) threaten the safety of our service men and women in military conflicts. These explosive devices not only produce substantial structural failure to the vehicle, but also create shock waves that are transmitted into the vehicle floor plate. The floor plate deflects in a span of microseconds, and the energy is transferred into the lower extremities of the occupants.[1] Recent military conflicts have seen an increased use of IEDs that has led to a rising number of severe injuries.[2,3] In fact, lower-extremity injuries accounted for more than a quarter of all combat injuries, with a third of those injuries caused by IEDs.[4] As such, lower-extremity injury prevention is of high concern but requires an improved understanding of the effect of biological and anatomical uncertainty and variability on lower-extremity fracture risk due to high-rate impact loading.

Cadaveric testing has been used in the past to study high-rate loading events but is limited by several drawbacks. Low availability of specimens, large variability in age, weight, and sex, difficulty in creating the impact, and the destructive nature of blast testing all hinder the applicability of cadaveric testing. To overcome these limitations, finite-element (FE) modeling has been used as a successful surrogate to evaluate injury risk. Numerous studies over the past two decades have investigated high-rate loading of the lower extremities using FE modeling. A large majority of these studies focused on automotive crashes in which the lower extremities experience a lower loading rate than an IED blast loading.[5–9] In the less common simulations with high loading rates and magnitudes, model geometries are generally restricted to dummy models or a single medical image set that corresponds to average males or females. For example, Nilakantan and Tabiei performed a numerical study investigating lower-extremity positioning during an IED blast in 2009 using a HYBRID III anthropomorphic test device (ATD) model.[10] Suresh et al. used the Wayne State University–validated ATD model in 2014[11] as did Dong et al. in 2013.[12] Fielding et al. used computed tomography (CT) images of a subject representing the 50th-percentile male in their blast simulation.[13] In perhaps two of the most convincing studies, Quenneville et al. developed an FE model[14] of their tibial impact apparatus[15] and validated the contact forces against their experimental data. In their experimental work using seven pairs of cadaveric tibias, they developed a fracture-risk curve that included a 10% of fracture with 7.9 kN. However, in their FE study and the previously mentioned studies, anatomical variability as well as variability and uncertainty in biological material properties have largely been ignored. Significant inter-individual variation limits the generalizability of conclusions based on such models. As such, protective equipment design, injury mitigation strategies, and the mechanics of tibial fracture can only be assessed on a population average basis. Probabilistic FE modeling combined with statistical-shape-modeling representations of human anatomy[16–24] provide a powerful framework to incorporate population-wide uncertainty and variation. The aforementioned studies and their major limitations can be improved by incorporating probabilistic methodologies.

In this work we perform a probabilistic analysis of high-rate lower extremity axial loading and compute a tibial fracture probability. Our analysis is an extension of Quenneville et al.[14,15] and an attempt to account for variability and uncertainty in bone shape, bone-mineral-density (BMD) distribution, material properties, and the inclusion of the talus. By accounting for natural physiological variation, we hypothesized that Quennneville et al.'s experimentally derived fracture risk can be reproduced in a computational framework. More specifically, we hypothesized that an axial contact force of 7.5 kN on the distal tibia in our probabilistic FE model will produce a fracture probability similar to the 10% risk associated with 7.9 kN of loading.[15] This study will provide several unique advantages for the advancement of IED blast injury mitigation strategies. Protective equipment and injury mitigation strategies can be rationally designed, and the overall reduction in population risk can be computed. Furthermore, probabilistic analysis can determine inputs to the system that are highly influential on fracture risk. These characteristics can be isolated, and individuals exhibiting these traits can be more readily identified as injury-prone or injury-resistant. Additionally, the framework described in this study allows for a quick and accurate implementation of an individual's bone geometry and density distribution into the probabilistic model. Therefore, injury prevention strategies and protective equipment can be designed on an individual basis, if warranted, depending on an individual's anatomical characteristics, and/or equipment can be designed to mitigate the most problematic inputs into the biomechanical system (low bone stiffness, for example). All of this can be done while accounting for uncertainty in the material properties and load magnitude of an individual bone, soft tissue, equipment, and so on. This work serves as the first study to model high-rate distal-tibia impacts probabilistically and develop a comprehensive tool for further research into injury prevention.

2. Methods

2.1 Overall Strategy

In this study, a statistical shape and density model (SSDM) was developed using cadaveric CT scans of the lower limb. The SSDM provided a means of generating physiologically plausible anatomies that captured the variation with the training set used to develop the model. Random variable descriptions of the material properties for the tibia were derived from literature and internal sources to account for the observed property variation. A distal-tibia impact simulation was developed following the methodology of Quenneville et al. using a tibial impact of approximately 7.5 kN, which corresponded to nearly a 10% tibial fracture risk.[15] Using the probabilistic descriptions of anatomy and material properties, a Latin Hypercube probabilistic FE analysis was performed to capture the distribution and uncertainty in each of the varying inputs. All simulations were performed using LS-DYNA (v. 970, Livermore Software Technology Corporation, Livermore, California). The methods are further described in the following.

2.2 Image Acquisition, Segmentation, and Mesh Preparation

This study is based on the experimental and computational work from Quenneville et al.[15] In their experimental study, older (41+ years of age) male cadavers were used to develop an injury risk curve with probability of fracture as a function of impact magnitude. As a means of comparison, the current study used the same demographic of individuals. As such, six older male (40+ years of age) cadaveric lower-body quantitative CT scans were provided by the Medical College of Wisconsin.

The CT scans were imported into Seg3D (SCI Institute, University of Utah) for segmentation.[25] A grayscale threshold filter was used to automatically segment the cortical boundaries of the tibia and talus, and the remaining unsegmented tibial and talus bone was subsequently filled using cavity fill and/or manual segmentation. These segmentations were exported in stl format to MeshLab open-source software.[26] Using MeshLab, each stl mesh (both the tibia and talus) was processed by the following:

1) Laplacian smoothing with three smoothing steps
2) Screened Poisson surface reconstruction with a reconstruction depth of 8, a minimum number of samples of one, and an interpolation weight of 4
3) Isoparametric remeshing with a sampling rate of 5

This processing sequence resulted in smooth, uniformly distributed surface triangular elements with similar mesh densities in each of the six specimens. Facet counts were reduced from approximately 200,000 to approximately 10,000 with minimal volume loss (Fig. 1). Sharp boundaries, such as the proximal tibial eminence, were smoothed slightly but deemed acceptable as a region of noninterest.

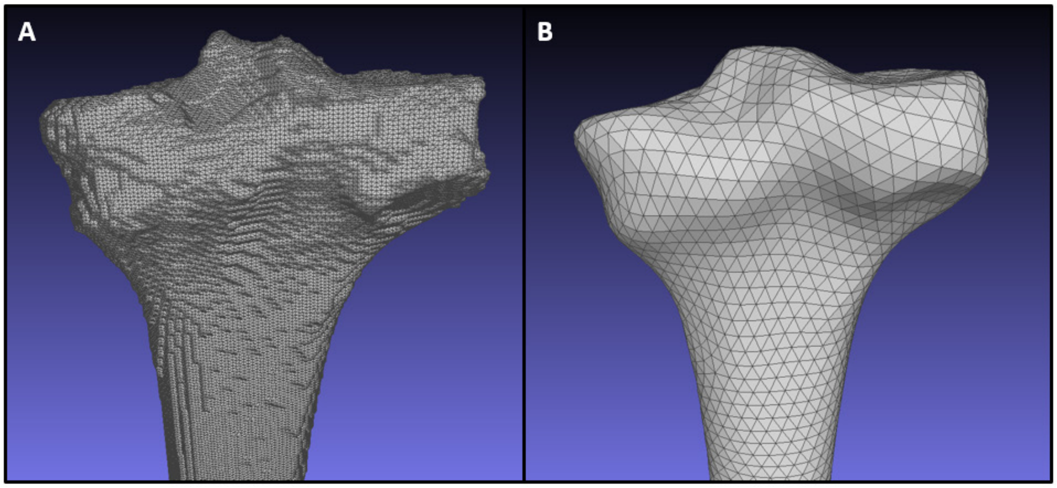

Fig. 1 A) Unprocessed exported mesh from Seg3D. B) Processed mesh using Meshlab. Minimal volume loss occurred with the processing and feature loss occurred in noninterest areas such as the proximal tibial eminence.

2.3 Mesh Correspondence and FE Meshing

Developing an SSDM requires that each geometry is represented by the same mesh with node-to-node anatomical correspondence.[27] This can be accomplished by choosing a template mesh and warping that to each of the remaining (five) meshes. To this end, a coherent point drift algorithm was implemented using a developed python module, pycpd (https://github.com/siavashk/pycpd), which resulted in six surface meshes with the same number of nodes and each node corresponding to a specific anatomical location (Fig. 2). This results in a high-fidelity parametric representation of the tibia anatomy with the nodes as the model parameters.

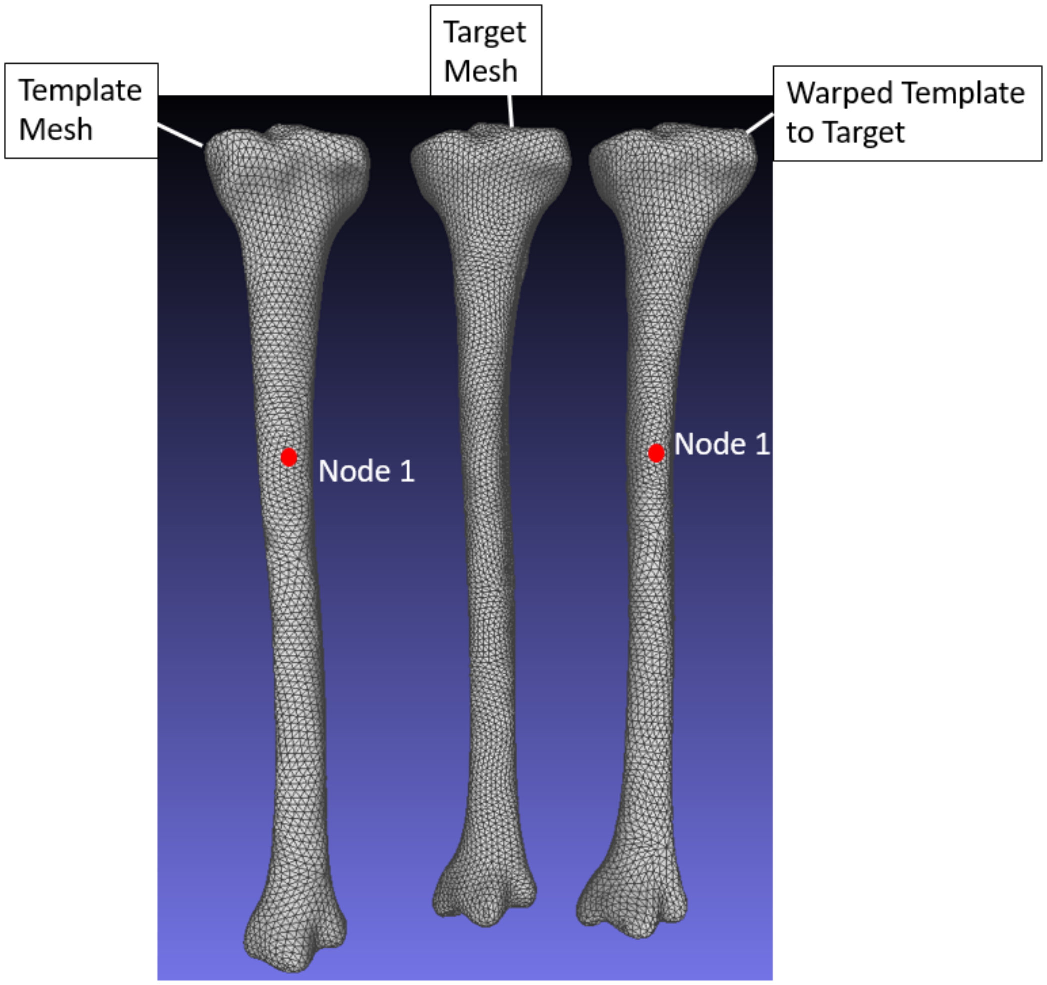

Fig. 2 Coherent point drift algorithm implemented using the python module, pycpd. One of the meshes was selected as the template mesh and was warped to each of the remaining five meshes with deformable registration. Anatomical correspondence is retained between nodes in each warped template mesh. Both the template tibia and talus were warped to each target mesh tibia and talus, but only the tibia is shown in this figure.

To develop FE meshes for each specimen, first the template mesh was imported into TrueGrid v3.1.3 (XYZ Scientific Inc, Livermore, California). A hexahedral mesh was developed (Fig. 3) by attaching TrueGrid "block-mesh" nodes to specific node numbers on the imported surface and then performing a sequence of general smoothing and mesh enhancement techniques. When a TrueGrid input file is generated, the node numbers are not stored; instead, the nodal coordinates are stored as the block-mesh attachment points. Therefore, the nodal numbers were noted that corresponded to the coordinates in the template TrueGrid input file. An internally developed python script was then used to search the stl ASCII file of each remaining mesh and replace the nodal coordinates in the template TrueGrid mesh file with the new nodal coordinates that correspond to the respective node number.

This provided an efficient method for automatic mesh generation that produced the same number of FE nodes and elements in the same anatomical positions across each mesh. Finally, Bonemat[28] was used to map Hounsfield units to ash densities for each FE mesh using their respective CT scan. Hounsfield units were converted to ash densities by use of a five-density calibration phantom (Mindways Software, Austin, Texas).

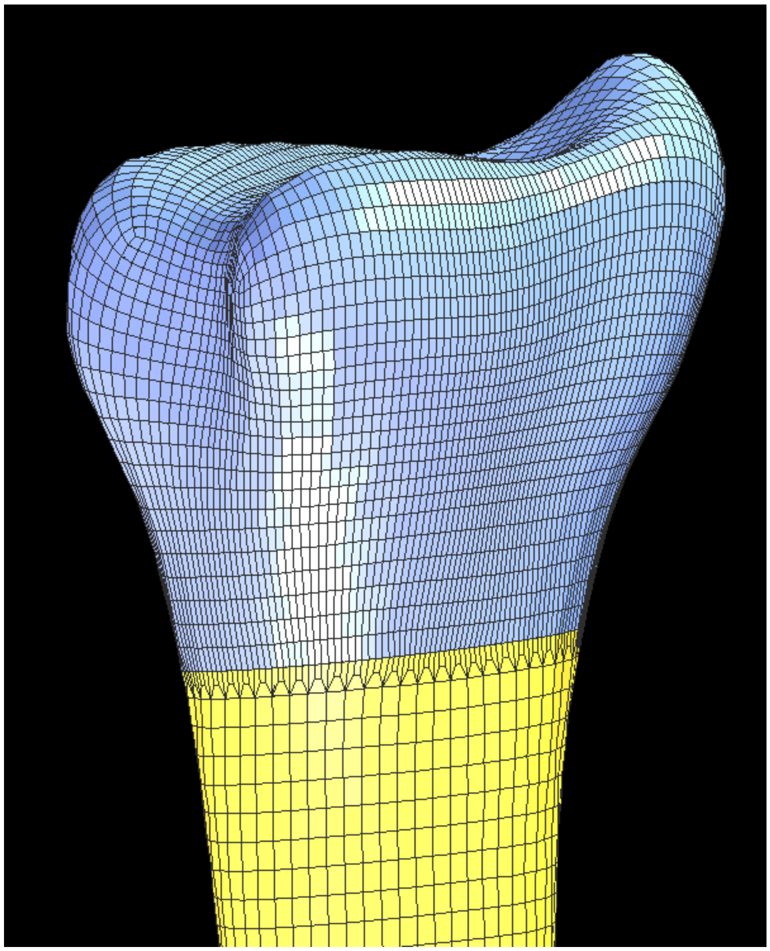

Fig. 3 Template volumetric FE mesh produced using TrueGrid. A mesh convergence study using the 2nd-percentile strain as the output of interest resulted in a mesh of approximately 200,000 elements with element edge lengths of 0.3–2.2 mm. The smallest elements were localized to the distal tibia.

2.4 Statistical Shape and Density Model

The FE mesh and corresponding element bone densities were described by a shape and density parameter vector as

$$\boldsymbol{p}_j = (v_{1x}, v_{1y}, v_{1z}, \dots, v_{jx}, v_{jy}, v_{jz}, v_{1d}, \dots, v_{ed}) \tag{1}$$

where $v_{1(xyz)}$ are the 3-D coordinates of the nodes in the FE mesh (tibia and talus); v_{ed} are the element densities (tibia only); $j = 1$ …, denotes each node in the FE mesh; $e = 1, \ldots,$ denotes each element in the tibia mesh; and $i = 1, \ldots, n = 6$ denotes each tibia/talus pair in the training set. Using these shape and density vectors and following the procedures of Nicolella and Bredbenner,[27] a parametric probabilistic representation of the tibia (shape and bone densities) and talus (shape) was developed. Two principal components (PCs) described 85% of the variation in the training set, with PC 1 and PC 2 describing 70% and 15% of the variation, respectively (Figs. 4 and 5). Statistically plausible anatomies were generated by varying the scalar weights (c_j) of each of the two PCs in Eq. 2:

$$\boldsymbol{p}_v = \overline{\boldsymbol{p}} + \sum_{j=1}^{m} c_j \sqrt{\lambda_j}\, \boldsymbol{q}_j \tag{2}$$

where $\boldsymbol{p}_v$ is a vector containing nodal coordinates and element ash densities for the FE mesh, m is the number of eigenvalues (length(λ_j) = 2), $\overline{\boldsymbol{p}}$ is the average shape and density vector, c_j is the scalar weighting factor, and $\boldsymbol{q}_j$ are eigenvectors.

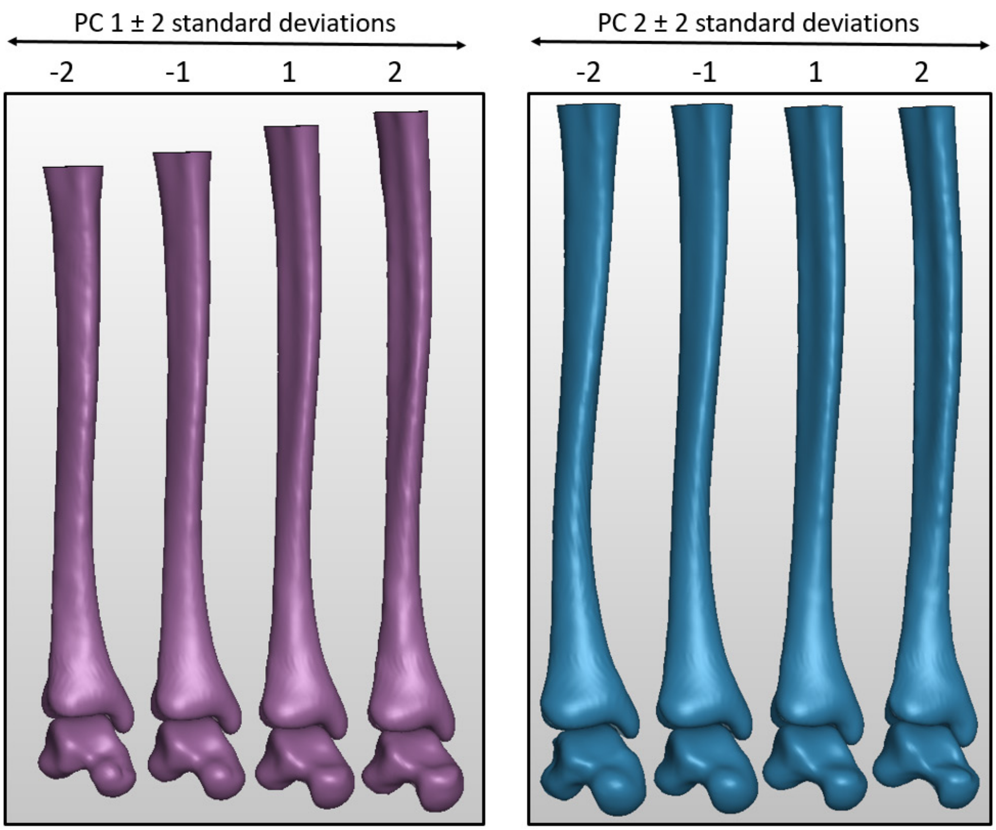

Fig. 4 PCs 1 (left) and 2 (right) describe 85% of the shape and density distribution variation contained in the six specimens. Shown are ±1 and 2 standard deviations from the average tibia/talus configuration (not shown). PC 1 primarily contained length and width variation in the tibia, as well as anterior talus size. PC 2 contained medial and lateral bend of the tibia, size of the medial malleolus, as well as slight ankle eversion/inversion variation.

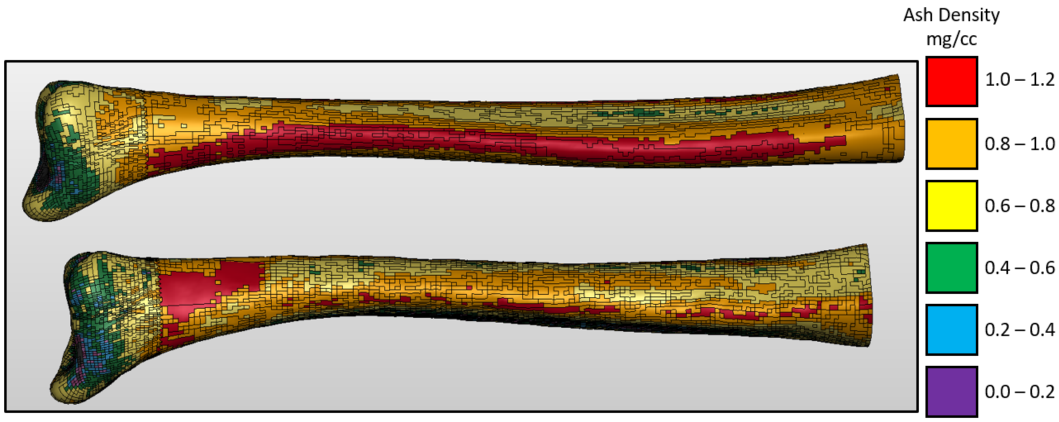

Fig. 5 Density distribution variation contained in both PCs, although primarily represented in PC 1. (top) +1.5 standard deviations of both principal components from the average model. (bottom) –1.5 standard deviations of both principal components from the average model.

2.5 Material Properties of the Tibia and Talus

The tibia-bone-material behavior was modeled as elastic–plastic with linear hardening using the LS-DYNA MAT_ELASTIC_PLASTIC,[29] which defines an elastic modulus and a plastic modulus (postyield behavior). The Cowper–Symonds model was implemented into the material definition (Eq. 3), which scales the yield stress with strain rate and accounts for marrow in the pores of trabecular bone[14,30]:

$$\sigma_y = \left[1 + \left(\frac{\dot{\varepsilon}^{1/P}}{C}\right)\right] * \sigma_0 \quad (3)$$

where σ_0 is the initial yield stress, $\dot{\varepsilon}$ is the strain rate, and *C* and *P* are the Cowper–Symonds parameters defined in this study as 360.7 and 4.605, respectively. The elastic modulus was defined probabilistically for each element using ash densities and data from Keller.[31] An example of how the variance in bone experimental data is captured statistically can be found in Fig. 6. Once the conversion was made, ash densities were scaled to apparent densities by the relationship $\rho_{app} = 0.6 * \rho_{ash}$. Hourglass control was implemented using Flanagan–Belytschko viscous form with exact volume integration and a coefficient of 0.1. Cortical bone failure was defined probabilistically as a maximum strain adapted from Reilly and Burstein.[32] Maximum strain was used as the failure criteria because of the implementation of plasticity in the material definition. Yield strain was defined probabilistically using internal unpublished bone-failure data. Finally, the plastic modulus was also defined probabilistically as a function of the elastic modulus. A summary of each varying input parameter including material properties can be found in Table 1.[31–33] The talus was modeled as rigid since the interest of this study was the risk of tibial fracture.

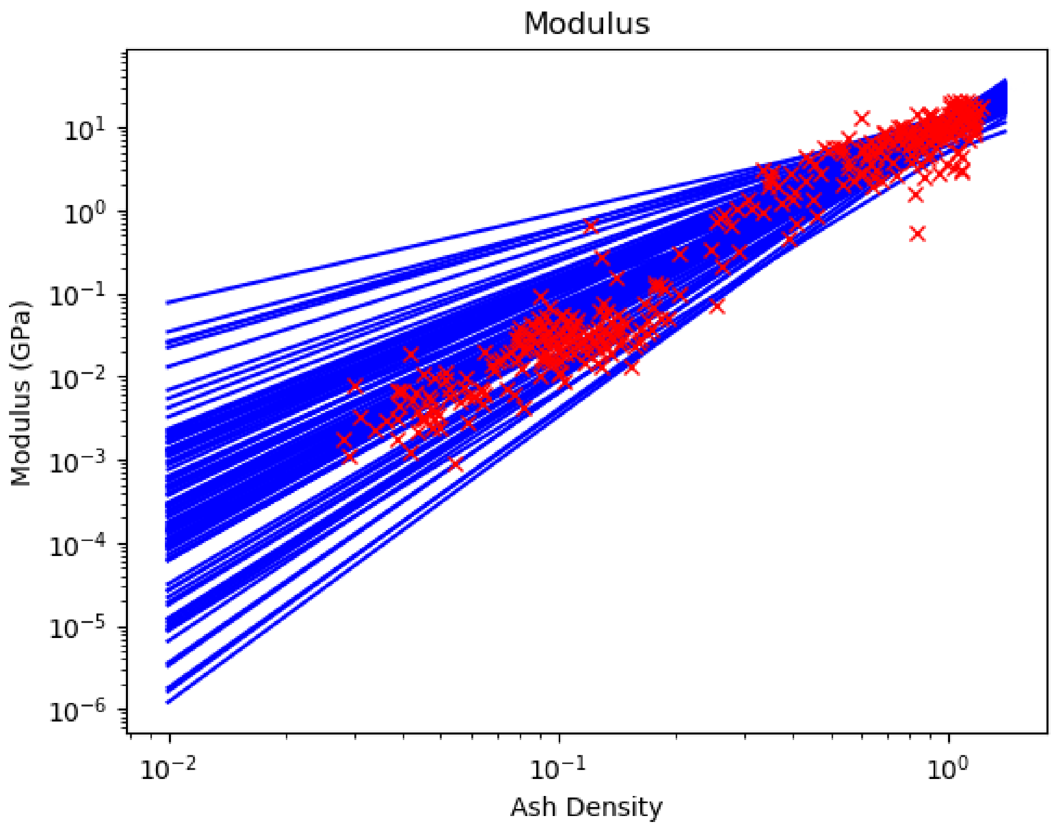

Fig. 6 **Log–log plot showing experimental data of ash density vs. modulus with red X's adapted from Keller 1994.[31] Blue lines show the Ax^b fit using normally distributed values for A and b taken from the same manuscript (Table 1). The majority of the red X's are contained within the normally distributed fits with slight error in the low moduli values given a high ash density.**

Table 1 **Summary of the varying inputs used in this study, their distribution, and their reference, if applicable. Log-normal distributions were used for a majority of the inputs to avoid negative values, which are nonphysiological for a majority of the inputs.**

	A	b	Yield Stress	PC 1	PC 2	Plastic Modulus	Failure Strain
Input	10500 ± 2000	2.29 ± 0.5	130 ± 23	0 ± 0.75	0 ± 0.75	0.06 ± 0.01	1.87% ± 0.29%
Unit	MPa	-	MPa	-	-	*Elastic Modulus	-
Distribution	log normal	log normal	log normal	normal	normal	log normal	log normal
Reference	Keller	Keller	Unpublished	-	-	Bayraktar	Reilly

2.6 Other Components

The impactor, distal bracket, and proximal bracket (Fig. 7) were modeled as rigid, while the foam was modeled as a low-density foam to increase the contact time between the talus and tibia. The material properties of the foam were not fitted to any experimental data but instead tuned to achieve the appropriate response that closely mimicked the results from Quenneville and Dunning.[14]

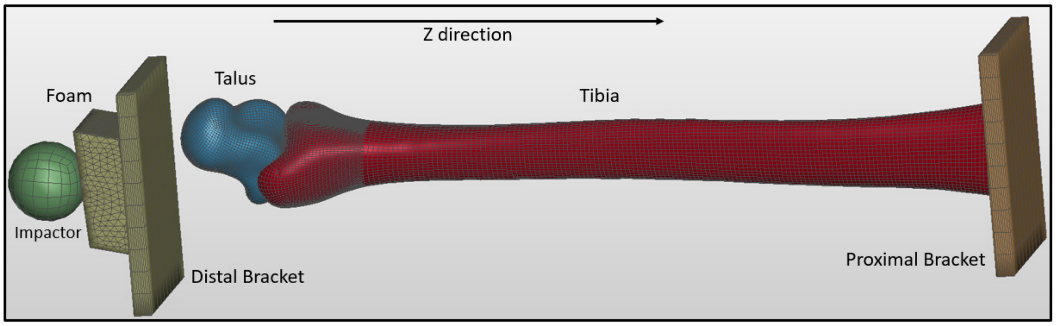

Fig. 7 Initial configuration of the simulation with the z-direction shown for reference to the listed boundary conditions. The tibia and talus in this example are taken as the average model, $\bar{\boldsymbol{p}}$.

2.7 Boundary Conditions

Starting from the right and moving to the left in Fig. 7, the boundary conditions were as follows. The proximal bracket was constrained in all motion except z-translation. The proximal tibia was removed to the diaphysis and rigidly tied to the proximal bracket. The nonrigidly tied portion of the tibia was free to rotate and translate in all 6 degrees of freedom. The talus was constrained in all motion except z-translation and was rigidly fixed to the movement of the distal bracket. The distal bracket was constrained in all motion except z-translation. The proximal nodes of the foam were rigidly tied to the distal bracket and could freely deform. The impactor was given an initial velocity in the z-direction, which was tuned to create a response that mimicked Quenneville and Dunning[14] and Quenneville et al.[15] Surface-to-surface contact was defined between the talus and tibia and also between the impactor and foam. In Fig. 8 the distal-tibia contact force as a function of time is plotted against experimental data from Quenneville and Dunning.

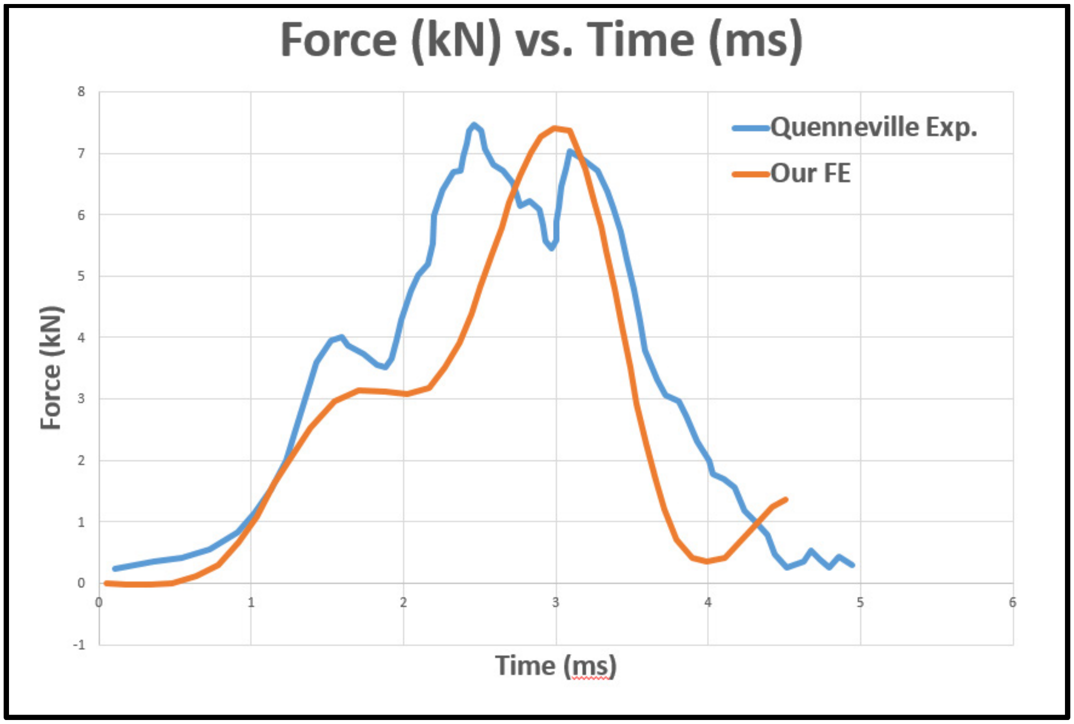

Fig. 8 Contact force on the distal tibia with the experimental study by Quenneville et al.[14,15] shown in blue, and our FE simulation of the average model shown in orange. The foam properties and initial velocity of the impactor were tuned to achieve similar contact force–time history. Peak force from our simulation was around 7.5 kN, slightly lower than the 7.9-kN force corresponding to a 10% fracture risk.[15]

2.8 Data Analysis

NESSUS probabilistic software (Southwest Research Institute, San Antonio, Texas) was used to perform the Latin Hypercube sampling of the varying inputs. A custom python script was written to access each simulation's output "elout" file, which contained element strains for all cortical bone elements (apparent density > 0.75) at each time step. The maximum effective strain, defined as $\sqrt{\frac{2}{3}\varepsilon_{ij}\varepsilon_{ij}}$ for each element, was calculated, and the final output response from each simulation was defined as the 2nd-percentile maximum effective strain. In other words, if 2% of the elements had maximum effective strain values above a failure threshold, failure would occur.[34,35] NESSUS generated the probabilistic response distribution alongside the failure criteria distribution and determined the probability of failure. This can be achieved by calculating the intersecting area of the failure-strain-criterion distribution with a response probability distribution (Fig. 9). Finally, NESSUS calculated the relative sensitivities of each input to the computed probabilistic response.

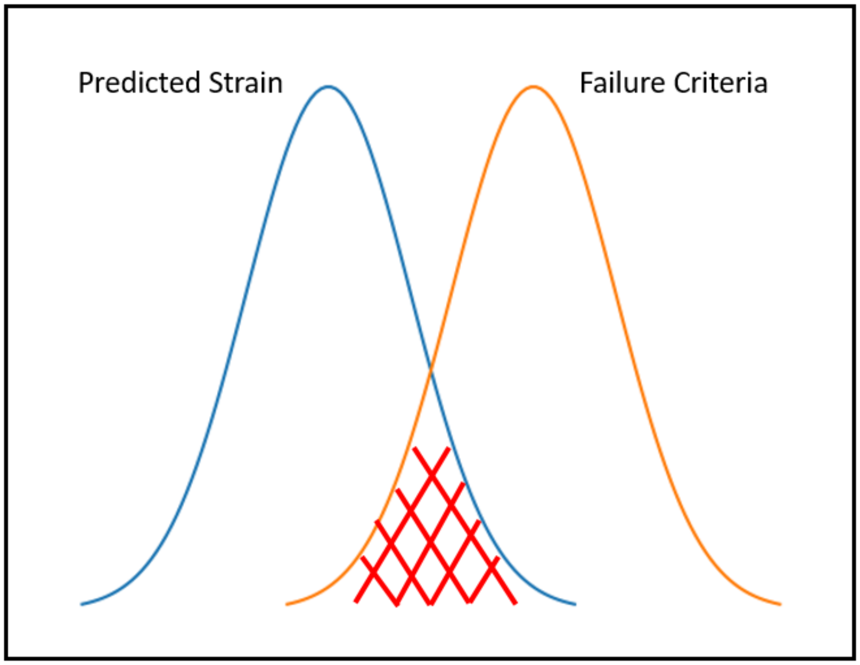

Fig. 9 In a probabilistic reliability analysis, the probability of failure is defined as the intersecting area between the probability of responses and failure criterion. In this study, the response is the 2nd-percentile maximum strain and the failure criterion is ultimate strain.

3. Results

All simulations ran to completion. Each simulation ran for about 4 h using two cores, and 10 simulations ran simultaneously. The total simulation time was less than 2 days.

In areas of interest, hourglass energy was less than 1% of the internal energy, and 2nd-percentile maximum effective strains varied from 0.4% to 5% (Fig. 10). Of 100 simulations, 10 resulted in fracture (10% probability of fracture with 7.5 kN of contact force on the distal tibia).

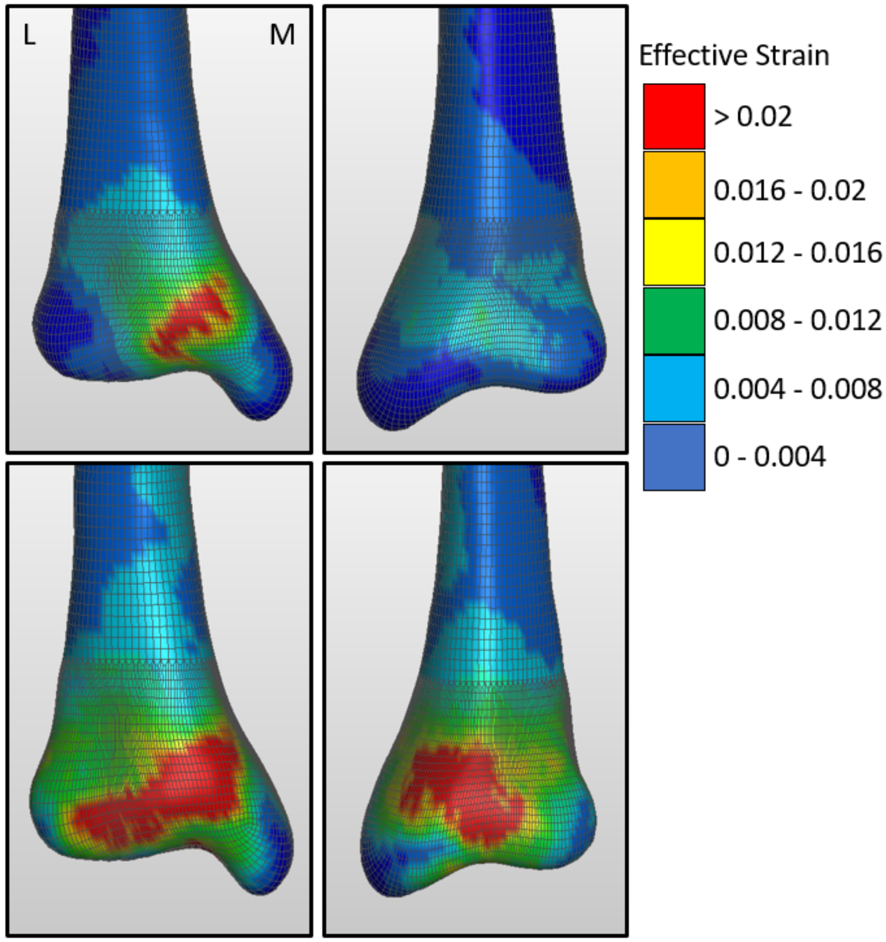

Fig. 10 (top row) Likely nonfracture case. (bottom row) Likely fracture case. The bottom tibia was longer and more slender but had similar material property mapping coefficients (A, b) to the top case. L denotes lateral, and M denotes medial. This case comparison demonstrates the importance of anatomical geometry and density distribution in tibial fracture risk.

The probability of fracture was most heavily influenced by the failure strain followed by the mapping of ash density to Young's modulus. Lower material properties were associated with a higher risk of fracture. To this end, a lower A value was predictive of fracture, while a higher b value was predictive of fracture (Ax^b). PC 1 of the SSDM and yield stress also had a significant effect on the computed risk of fracture. Longer, slender bones were more likely to fail than shorter, more-robust bones. The plastic modulus and PC 2 had the lowest influence on the probability of fracture (Fig. 11).

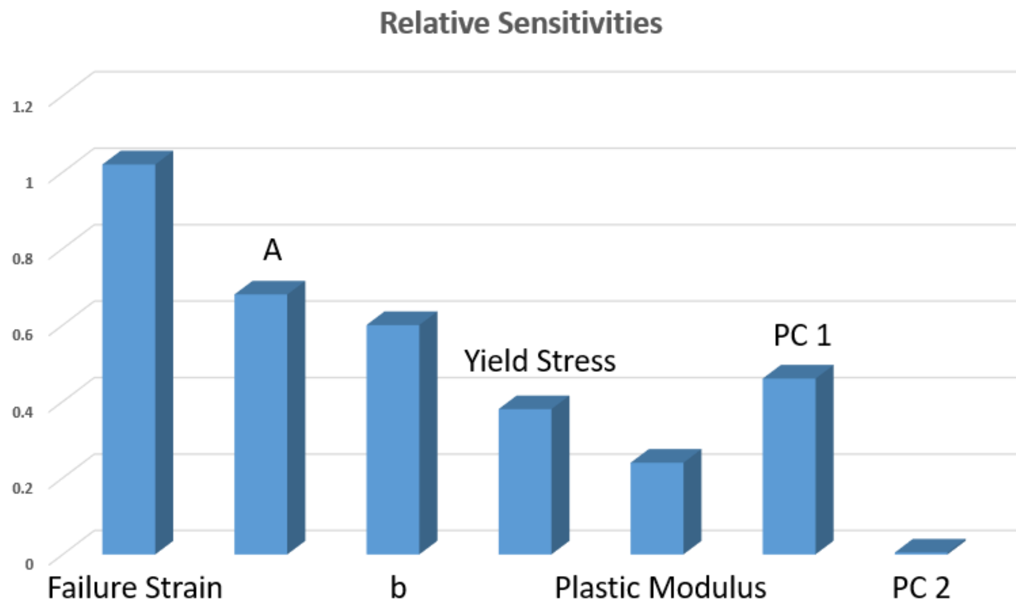

Fig. 11 Relative sensitivities of each of the varying inputs to the 2nd-percentile maximum effective strain

4. Discussion and Conclusion

In this study, we described and implemented a probabilistic FE modeling workflow for high-rate distal-tibia impact that accounts for both uncertainty and variability in biological material properties and anatomical variation within a population. We have demonstrated that our probabilistic methodology is able to produce the tibial fracture risk developed from high-rate-loading experimental studies. This study design was an extension of work for a direct comparison of fracture risk prediction, although our study included the talus to provide a more physiologic load transfer into the tibia. In Quenneville et al.'s experimental work,[14,15] an impact force of 7.9 kN was found to correspond with a 10% risk of fracture. Our probabilistic model produced a 10% fracture risk for a similar contact force of 7.5 kN, which is in agreement with Quenneville et al. and supports our probabilistic methodology. As such, we can investigate the influence of each probabilistic input on the computed probability of fracture.

Probabilistic FE modeling provides a thorough analysis of the sensitivities of the output response to the probabilistic inputs. This is important in protective equipment design, individual risk assessment, and targeted training/risk-mitigation programs. Once identified, risk-mitigation strategies can be focused on those variables that most influence the risk of injury. In this study, the most important variable that influenced fracture risk was bone failure strain. This is not surprising but does reinforce the importance of developing bone failure criteria. Simple measures of stress and strain may be inadequate to describe bone failure. In Wolfram and Schwiedrzik's summary paper of failure properties in cortical bone,[36] dozens of experimental bone failure studies demonstrate the equivocality of bone failure. Across all studies,[32,33,37–55] failure properties of cortical bone show enormous variance based on age of bone, type of loading, modulus estimation strategy, and even substantial intravariance within each study. In this study, we chose one experimental study based on age of donors and axis of loading.[32]

Another unsurprising result from this study was that material stiffness strongly predicted bone fracture. Individuals with lower bone stiffness experienced larger strains, significantly increasing their risk of fracture. However, interestingly, this translates to a lower exponent in the Ax^b mapping. A higher b value predicting fracture can be explained by the large amount of cortical bone elements at the distal tibia with BMDs in the range of 0.75–1.0 g/cc. With values less than 1, a higher exponent would generate a lower modulus. As such, in the area prone to fracture, raising the exponent lowered the material properties using an Ax^b mapping.

Comparable to material properties, tibia anatomical geometry and bone density distribution had a large effect on fracture risk. Consistent with Jepsen's findings of robust versus slender bones, we found that long, thinner bones were significantly associated with fracture, whereas shorter, wider bones were not.[56,57] Longer bones were associated with higher BMD along the tibial diaphysis, though in this study higher BMD did not sufficiently compensate for the larger bending observed in these bones at the distal-tibial neck. These results demonstrate that certain individuals are more prone to severe injury based on their anatomy alone. Medial and lateral tibial bend, as well as slight ankle eversion and inversion captured in PC 2 did not have a significant effect on the results of this study.

Several limitations in this work limit its applicability. Only six CT scans were used to generate the SSDM, which limits the anatomical variation captured among the population. Moreover, these scans were from older (age 50+) males, thus neither reliably represent younger bone's density distribution nor include the female response (both of which would be at risk in a military conflict). Younger bones would presumably have higher BMD, which would offer more protection to the loading blast and may reduce the fracture risk calculated in this study. Females should be modeled in a separate probabilistic study, as many differences exist between sexes and are worth separating for fracture risk prediction and mitigation strategy. Another limitation is our choice of 2nd-percentile strain as the failure criterion. By choosing a higher or lower percentile, the probability of failure was changed accordingly. While our choice is based on an empirically determined value, there is uncertainty in its general use. The strain percentile as a failure criterion could be statistically represented in the same probabilistic manner to account for this uncertainty. This study also did not include many of the anatomical features of the lower extremity. Cartilage was not included and neither were the fibula, bones of the foot, ligaments, and musculature. These structures would offer additional support to the load and would likely reduce the fracture risk. Therefore, the 10% fracture risk for a 7.5-kN distal-tibial load produced in this study is likely a conservative estimate. Nonetheless, this study was developed as a direct comparison with an existing experimental study and, to that end, illustrates the capabilities of probabilistic analysis applied to human body modeling. This study can be further improved to include the additional anatomical structures and a more representative demographic. A more accurate and comprehensive risk of injury could be determined with the suggested improvements.

The major strengths of this study include the close agreement with experimental data and the described methodology as a general probabilistic workflow. To the authors' knowledge, no computational model has been developed that can comprehensively produce an experimentally derived probability of tibial fracture in high-rate loading scenarios. By accounting for natural variation between individuals and accurately capturing the probability of injury, our model functions as a suitable surrogate to cadaveric testing in the described loading conditions. Protective equipment and injury mitigation strategies can be rationally developed using this model. Along with the immediate strengths of this model, the workflow described herein can be used in many other analyses that have inherent uncertainty and variation.

In conclusion, we developed a probabilistic FE model that accurately captures the fracture risk developed from experimental work. We have demonstrated the utility of probabilistic methodologies for assessing distal-tibia high-rate-impact events such as IED blast loading. This methodology can be used with a demographic that represents military personnel that would most likely be in a combat situation. As such, that model could be used to develop protective equipment and/or identify at-risk individuals. Ultimately, this model and models developed hereafter may assist in lowering the incidence rates of severe lower-extremity injuries during military conflicts.

5. References

1. Arepally S, Gorsich D, Hope K, Gentner S, Dotleff K. Application of mathematical modeling in potentially survivable blast threats in military vehicles. Proceedings of the 26th Army Science Conference; 2008 Dec.

2. Greer N, Sayer N, Kramer M, Koeller E, Velasquez T. VA Evidence-based synthesis program reports. Prevalence and epidemiology of combat blast injuries from the military cohort: 2001–2014. Washington (DC): Department of Veterans Affairs (US); 2016.

3. Ramasamy A, Newell N, Masouros S. From the battlefield to the laboratory: the use of clinical data analysis in developing models of lower limb blast injury. J R Army Med Corps. 2014;160(2):117–120.

4. McKay BJ, Bir CA. Lower extremity injury criteria for evaluating military vehicle occupant injury in underbelly blast events. Stapp Car Crash Journal. 2009;53:229–249.

5. Beillas P, Begeman PC, Yang KH, King AI, Arnoux PJ, Kang HS, Kayvantash K, Brunet C, Cavallero C, Prasad P. Lower limb: advanced FE model and new experimental data. Stapp Car Crash Journal. 2001;45:469–494.

6. Kim YS, Choi HH, Cho YN, Park YJ, Lee JB, Yang KH, King AI. Numerical investigations of interactions between the knee-thigh-hip complex with vehicle interior structures. Stapp Car Crash Journal. 2005;49:85–115.

7. Iwamoto M, Tamura A, Furusu K, Kato C, Miki K, Hasegawa J, Yang KH. Development of a finite element model of the human lower extremity for analyses of automotive crash injuries. SAE Transactions. 2000;109:846–853.

8. Takahashi Y, Kikuchi Y, Konosu A, Ishikawa H. Development and validation of the finite element model for the human lower limb of pedestrians. Stapp Car Crash Journal. 2000;44:335–355.

9. Untaroiu C, Darvish K, Crandall J, Deng B, Wang JT. A finite element model of the lower limb for simulating pedestrian impacts. Stapp Car Crash Journal. 2005;49:157–181.

10. Nilakantan G, Tabiei A. Computational assessment of occupant injury caused by mine blasts underneath infantry vehicles. Int J Veh Struct Sys. 2009;1:50–58.

11. Suresh M, Zhu F, Yang K, Serres J, Tannous R. Finite element evaluation of human body response to vertical impulse loading; 2014 [accessed 2020 June 30]. doi: 10.5151/meceng-wccm2012-18555.

12. Dong L, Zhu F, Jin X, Suresh M, Jiang B, Sevagan G, Cai Y, Li G, Yang KH. Blast effect on the lower extremities and its mitigation: a computational study. J Mech Behav Biomed Mater. 2013;28:111–124.

13. Fielding RA, Kraft RH, Przekwas A, Tan XG. Development of a lower extremity model for high strain rate impact loading. Int J Exper Computa Biomech. 2015;3(2):161–186.

14. Quenneville CE, Dunning CE. Development of a finite element model of the tibia for short-duration high-force axial impact loading. Comput Methods Biomech Biomed Engin. 2011;14(2):205–212.

15. Quenneville CE, McLachlin SD, Greeley GS, Dunning CE. Injury tolerance criteria for short-duration axial impulse loading of the isolated tibia. Journal of Trauma. 2011;70(1):E13–18.

16. Bredbenner TL, Eliason TD, Francis WL, McFarland JM, Merkle AC, Nicolella DP. Development and validation of a statistical shape modeling-based finite element model of the cervical spine under low-level multiple direction loading conditions. Front Bioeng Biotechnol. 2014;2:58.

17. Coombs DJ, Rullkoetter PJ, Laz PJ. Efficient probabilistic finite element analysis of a lumbar motion segment. J Biomech. 2017;61:65–74.

18. Francis W, Eliason T, Thacker B, Paskoff G, Shender B, Nicolella D. Implementation and validation of probabilistic models of the anterior longitudinal ligament and posterior longitudinal ligament of the cervical spine. Computer Methods in Biomechanics and Biomedical Engineering. 2012;17.

19. Francis WL, Nicolella DP, Popelar CF, Thacker BH. Probabilistic-based modeling and simulation assessment. Warren (MI): Army TARDEC (US); 2010. Report No.: TFLRF 408. p. 38.

20. Laz PJ, Stowe JQ, Baldwin MA, Petrella AJ, Rullkoetter PJ. Incorporating uncertainty in mechanical properties for finite element-based evaluation of bone mechanics. J Biomech. 2007;40(13):2831–2836.

21. Myers CA, Laz PJ, Shelburne KB, Davidson BS. A probabilistic approach to quantify the impact of uncertainty propagation in musculoskeletal simulations. Ann Biomed Eng. 2015;43(5):1098–1111.

22. Thacker B, Wu Y-T, Nicolella D, Anderson R. Probabilistic injury analysis of the cervical spine. Proceedings of the 38th Structures, Structural Dynamics, and Materials Conference; 2012.

23. Wille H, Rank E, Yosibash Z. Prediction of the mechanical response of the femur with uncertain elastic properties. J Biomech. 2012;45(7):1140–1148.

24. Lu YC, Untaroiu CD. Statistical shape analysis of clavicular cortical bone with applications to the development of mean and boundary shape models. Comput Meth Prog Biomed. 2013;111(3):613–628.

25. Center for Integrative Biomedical Computing, Scientific Computing and Imaging Institute. Seg3D: volumetric image segmentation and visualization. http://www.sci.utah.edu/cibc-software/seg3d.html.

26. Cignoni P, Callieri M, Corsini M, Dellepiane M, Ganovelli F, Ranzuglia G. MeshLab: an open-source mesh processing tool; 2008 [accessed 2020 June 30]. http://vcg.isti.crn.it/Publications/2008/CCCDGR08/MeshLabEGIT.final pdf.

27. Nicolella DP, Bredbenner TL. Development of a parametric finite element model of the proximal femur using statistical shape and density modeling. Comput Methods Biomech Biomed Engin. 2012;15(2):101–110.

28. Taddei F, Schileo E, Helgason B, Cristofolini L, Viceconti M. The material mapping strategy influences the accuracy of CT-based finite element models of bones: an evaluation against experimental measurements. Med Eng Phys. 2007;29(9):973–979.

29. Hallquist JO. LS-DYNA keyword user's manual, Version 971. Livermore (CA): Livermore Software Technology Corporation; 2007.

30. Cowper GR, Symonds PS. Strain-hardening and strain-rate effects in the impact loading of cantilever beams. Providence (RI): Brown University, Division of Mathematics; 1957. Report No.: 28.

31. Keller TS. Predicting the compressive mechanical behavior of bone. J Biomech. 1994;27(9):1159–1168.

32. Reilly DT, Burstein AH. The elastic and ultimate properties of compact bone tissue. J Biomech. 1975;8(6):393–405.

33. Bayraktar HH, Morgan EF, Niebur GL, Morris GE, Wong EK, Keaveny TM. Comparison of the elastic and yield properties of human femoral trabecular and cortical bone tissue. J Biomech. 2004;37(1):27–35.

34. Boutroy S, Van Rietbergen B, Sornay-Rendu E, Munoz F, Bouxsein ML, and Delmas PD. Finite element analysis based on in vivo HR-pQCT images of the distal radius is associated with wrist fracture in postmenopausal women. Journal of Bone and Mineral Research. 2008;23(3):392–399.

35. Pistoia W, van Rietbergen B, Lochmuller EM, Lill CA, Eckstein F, Ruegsegger P. Estimation of distal radius failure load with micro-finite element analysis models based on three-dimensional peripheral quantitative computed tomography images. Bone. 2002;30(6):842–848.

36. Wolfram U, Schwiedrzik J. Post-yield and failure properties of cortical bone. Bonekey Rep. 2016;5:829.

37. Carter DR, Caler WE, Spengler DM, Frankel VH. Fatigue behavior of adult cortical bone: the influence of mean strain and strain range. Acta Orthopaedica Scandinavica. 1981;52(5):481–490.

38. Cezayirlioglu H, Bahniuk E, Davy DT, Heiple KG. Anisotropic yield behavior of bone under combined axial force and torque. J Biomech. 1985;18(1):61–69.

39. Courtney AC, Hayes WC, Gibson LJ. Age-related differences in post-yield damage in human cortical bone: experiment and model. J Biomech. 1996;29(11):1463–1471.

40. Currey JD. Tensile yield in compact bone is determined by strain, post-yield behavior by mineral content. J Biomech. 2004;37(4):549–556.

41. Dickenson RP, Hutton WC, Stott JR. The mechanical properties of bone in osteoporosis. J Bone Joint Surg Br. 1981;63-b(2):233–238.

42. Dong XN, Acuna RL, Luo Q, Wang X. Orientation dependence of progressive post-yield behavior of human cortical bone in compression. J Biomech. 2012;45(16):2829–2834.

43. Dong XN, Luo Q, Wang X. Progressive post-yield behavior of human cortical bone in shear. Bone. 2013;53(1):1–5.

44. Duchemin L, Bousson V, Raossanaly C, Bergot C, Laredo JD, Skalli W, Mitton D. Prediction of mechanical properties of cortical bone by quantitative computed tomography. Med Eng Phys. 2008;30(3):321–328.

45. Ebacher V, Wang R. A Unique Microcracking process associated with the inelastic deformation of Haversian bone. Advanced Functional Materials. 2009;19(1):57–66.

46. Evans FG. Mechanical properties and histology of cortical bone from younger and older men. Anat Rec. 1976;185(1):1–11.

47. Jepsen KJ, Davy DT. Comparison of damage accumulation measures in human cortical bone. J Biomech. 1997;30(9):891–894.

48. Lee SC, Coan BS, Bouxsein ML. Tibial ultrasound velocity measured in situ predicts the material properties of tibial cortical bone. Bone. 1997;21(1):119–125.

49. Leng H, Dong XN, Wang X. Progressive post-yield behavior of human cortical bone in compression for middle-aged and elderly groups. J Biomech. 2009;42(4):491–497.

50. Mirzaali MJ, Schwiedrzik JJ, Thaiwichai S, Best JP, Michler J, Zysset PK, Wolfram U. Mechanical properties of cortical bone and their relationships with age, gender, composition and microindentation properties in the elderly. Bone. 2016;93:196–211.

51. Nyman JS, Roy A, Reyes MJ, Wang X. Mechanical behavior of human cortical bone in cycles of advancing tensile strain for two age groups. J Biomed Mater Res A. 2009;89(2):521–529.

52. Reilly DT, Burstein AH, Frankel VH. The elastic modulus for bone. J Biomech. 1974;7(3):271–275.

53. Tang T, Ebacher V, Cripton P, Guy P, McKay H, Wang R. Shear deformation and fracture of human cortical bone. Bone. 2015;71:25–35.

54. Turner CH, Wang T, Burr DB. Shear strength and fatigue properties of human cortical bone determined from pure shear tests. Calcif Tissue Int. 2001;69(6):373–378.

55. Wang X, Nyman JS. A novel approach to assess post-yield energy dissipation of bone in tension. J Biomech. 2007;40(3):674–677.

56. Jepsen KJ, Evans R, Negus CH, Gagnier JJ, Centi A, Erlich T, Hadid A, Yanovich R, Moran DS. Variation in tibial functionality and fracture susceptibility among healthy, young adults arises from the acquisition of biologically distinct sets of traits. J Bone Miner Res. 2013;28(6):1290–1300.

57. Tommasini SM, Nasser P, Schaffler MB, Jepsen KJ. Relationship between bone morphology and bone quality in male tibias: implications for stress fracture risk. J Bone Miner Res. 2005;20(8)1372–1380.

List of Symbols, Abbreviations, and Acronyms

3-D	three-dimensional
ARL	Army Research Laboratory
ATD	anthropomorphic test device
Ax^b	fracture
BMD	bone mineral density
CCDC	US Army Combat Capabilities Development Command
CT	computed tomography
FE	finite element
IED	improvised explosive device
PC	principal component
SSDM	statistical shape and density model

1 (PDF) DEFENSE TECHNICAL INFORMATION CTR
DTIC OCA

1 (PDF) CCDC ARL
FCDD RLD CL
TECH LIB

11 (PDF) NATICK SOLDIER RSRCH DEV AND ENGRNG CTR
M G CARBONI
D COLANTO
C DOONA
R DILALLA
B FASEL
J FONTECCHIO
B KIMBALL
J KIREJCZYK
M MAFEO
M MARKEY
D PHELPS

4 (PDF) PROG EXECUTIVE OFC SOLDIER
E BEAUDOIN
J MULLENIX
J HOPPING
G WHITEHEAD

2 (PDF) US ARMY TEST AND EVALUATION COMMAND
A FOURNIER
R SPINK

1 (PDF) AUTO CELL PEO LAND SYS
A PURTELL

2 (PDF) OFFICE OF NAVAL RESEARCH
T BENTLEY
K YANKASKAS

1 (PDF) NAVAIR PATUXENT RIVER
B SHENDAR

6 (PDF) MRMC DOD BLAST INJURY RSRCH PROG COORDINATING OFC
R GUPTA
M LEGGIERI
R SHOGE
S HINDS
C STEELE
T PIEHLER

1 (PDF) MRMC JTAPIC PRGM OFC
J USCILOWICZ

3 (PDF) US ARMY AEROMEDICAL RSRCH LAB
F BROZOSKI
V CHANCEY
B MCENTIRE

1 (PDF) US AIR FORCE
C PIRNSTILL

1 (PDF) TARDEC
R SCHERER

1 (PDF) RDECOM HQ
AMSRD PE
D RUSIN

1 (PDF) EDGEWOOD CHEML AND BIOL RSRCH DEV AND ENG CTR
M HORSMON

1 (PDF) OSD DOT&E
J IVANCIK

45 (PDF) CCDC ARL
FCDD RLW
A RAWLETT
S SCHOENFELD
J ZABINSKI
FCDD RLW P
R FRANCART
FCDD RLW L
T V SHEPPARD
FCDD RLW M
E CHIN
FCDD RLW B
P GILLICH
C HOPPEL
A TONGE
L VARGAS-GONZALEZ
FCDD RLW MA
E WETZEL
T PLAISTED
FCDD RLW LH
J NEWILL
C GOOD
T THOMAS
A WEGENER
L MAGNESS
FCDD RLW PA
S BILYK
FCDD RLW PB
S ALEXANDER

T BAUMER
A BROWN
B FAGAN
A GOERTZ
A GUNNARSSON
C HAMPTON
R KARGUS
D KRAYTERMAN
M KLEINBERGER
E MATHEIS
J MCDONALD
P MCKEE
K RAFAELS
S SATAPATHY
M TEGTMEYER
K WEAVER
T WEERASOORIYA
S WOZNIAK
T ZHANG
FCDD RLW PC
M FERMEN-COKER
FCDD RLW PD
J RUNYEON
FCDD RLW PE
B AYDELOTTE
P SWOBODA
FCDD RLW PF
N GNIAZDOWSKI
E FIORAVANTE
FCDD RLW PG
J STEWART